

# Subpixel-Pixel-Superpixel Guided Fusion for Hyperspectral Anomaly Detection

Zhihong Huang<sup>1</sup>, Student Member, IEEE, Leyuan Fang<sup>1</sup>, Senior Member, IEEE, and Shutao Li<sup>1</sup>, Fellow, IEEE

**Abstract**—Most of the existing hyperspectral anomaly detectors are designed based on a single pixel-level feature. These detectors may not adequately utilize spectral–spatial information in hyperspectral images (HSIs) for detecting anomalies. To overcome this problem, this article introduces a novel subpixel-pixel-superpixel guided fusion (SPSGF) method for hyperspectral anomaly detection. This approach comprises three main steps. First, subpixel-, pixel-, and superpixel-level features are extracted from an HSI by employing the spectral unmixing, morphological operation, and superpixel segmentation techniques, respectively. Then, based on the spatial consistency of three features, a guided filtering-based weight optimization technique is developed to construct weight maps for fusion. Finally, a simple yet effective decision fusion method is adopted to utilize the complementary information of three features, and then generates a fused detection result. The performance of the proposed approach is evaluated on three real-scene HSIs and one synthetic HSI. Experimental results validate the advantages of the SPSGF method.

**Index Terms**—Anomaly detection, guided filtering, hyperspectral images (HSIs), image fusion, subpixel.

## I. INTRODUCTION

**H**YPERSPECTRAL images (HSIs) contain a wealth of spectral information, which can identify spectral signatures of various land coverings [1]–[3]. Therefore, HSIs have been widely used in many applications, including classification, visualization, and target detection [4]–[6]. Recently, hyperspectral anomaly detection has attracted much attention, since it plays a significant role in public safety and defense domains [7], [8].

In the remote sensing field, anomaly pixels usually have distinct spectral–spatial difference with their surrounding background pixels [9]. Hyperspectral anomaly detection aims to distinguish anomalies from their surrounding background without any prior information about anomalies [10]. During the past decades, many anomaly detection techniques

have been proposed [11]. Statistical modeling [12] and representation-based modeling [13] are two main strategies for the current detectors. Statistical modeling techniques are usually connected with Gaussian distribution. In [14], the Reed–Xiaoli (RX) algorithm uses a multivariate Gaussian model to estimate anomalies. Besides, some variants of the RX detector have been designed [15]–[20]. In [15], the regularized-RX method regularizes the local covariance matrix estimated from all pixels. In [16], the weighted-RX method is proposed to calculate the mean vector and covariance matrix with a Gaussian probability estimation. In [17], the kernel RX algorithm exploits the higher feature to strengthen the detection ability [18]. The cluster-based anomaly detection (CBAD) method [19] segments the scene into different regions and then identifies anomalies in each region. Moreover, some non-RX-based detectors have been proposed, including nonlinear learning-based detector [21], discriminative metric learning-based detector [22], and probabilistic anomaly detector [23].

Besides, representation-based modeling approaches also have attracted lots of attention [24]. These techniques suppose that the background can be constructed by some main spectra, while anomaly targets fail to. Sparse representation [25], [26], low-rank and sparse matrix decomposition (LRSMD) [27], [1], and tensor representation-based detectors [6] have been developed in recent years. In [25], the background joint sparse representation detector (BJSRD) utilizes the redundant background information to deal with complicated multiple background classes. In [26], background pixels can be constructed by their spatial neighborhood pixels, whereas targets fail to be well represented. In [27], the LRSMD method supposes that the background component is low-rank, and the remaining component can preserve anomalies. Since tensor models can well represent a three dimension data, a tensor representation-based detector is designed to detect anomalies [6]. Generally speaking, most of the current anomaly detectors are designed based on a single pixel-level feature, which may not fully capture spectral–spatial information in HSIs.

In fact, due to the low spatial resolution, HSIs target detection and scene classification often encounter a tough problem, i.e., the presence of mixed pixels. That is, a single pixel is jointly occupied by several distinct pure materials (endmembers), resulting in some severe problems for the accurate interpretation of the image contents [28], [29]. Fortunately, some unmixing approaches [30]–[32] have been designed to compute abundance fractions (AFs) of endmembers. With the

Manuscript received November 2, 2018; revised August 4, 2019 and September 29, 2019; accepted December 6, 2019. This work was supported in part by the National Natural Science Foundation of China for International Cooperation and Exchanges under Grant 61520106001 and in part by the Fund of Hunan Province for Science and Technology Plan Project under Grant 2017RS3024. (Corresponding author: Shutao Li.)

The authors are with the College of Electrical and Information Engineering, Hunan University, Changsha 410082, China, and also with the Key Laboratory of Visual Perception and Artificial Intelligence of Hunan Province, Hunan University, Changsha 410082, China (e-mail: zhih\_huang@hnu.edu.cn; fangleyuan@gmail.com; shutao\_li@hnu.edu.cn).

Color versions of one or more of the figures in this article are available online at <http://ieeexplore.ieee.org>.

Digital Object Identifier 10.1109/TGRS.2019.2961703

computed AFs, we can describe spectral mixture information at a subpixel level [33], [34]. On the other hand, some superpixel-based HSIs classification techniques [35], [36] have recently attracted much attention. Each superpixel in HSIs can be regarded as a set of pixels with similar spatial and spectral characteristics in a shape-adaptive homogeneous region [36]. A superpixel-level feature contains spectral–spatial similarity information, which has demonstrated to be useful for improving HSIs classification performance [37], [38]. In summary, the subpixel- and superpixel-level features contain the unique spectral–spatial information respectively, and provide complementary information for image interpretation and analysis.

Based on the analysis above, we propose a novel subpixel-superpixel guided fusion (SPSGF) method to exploit the complementary information among the subpixel-, pixel-, and superpixel-level features for hyperspectral anomaly detection. The proposed detector has three main steps. First, a spectral unmixing approach [39] is employed to calculate the AFs of endmembers, exploiting the spectral mixture information at the subpixel-level feature. By using the morphological operation [40], the spatial structure information can be exploited at the pixel-level feature. An entropy rate segmentation technique is adopted to exploit the spectral–spatial similarity information at the superpixel-level feature. Then, based on the spatial context of three complementary features, a guided filtering-based weight construction technique is developed to construct weight maps for fusion. Lastly, a simple yet effective decision fusion method is adopted to utilize complementary information of three features, and then generates a fused detection result.

The rest of this article is summarized as follows. We review the LRSMD and the guided filter in Section II. The proposed SPSGF method is introduced in Section III. Section IV presents the experimental results. Section V concludes this article with some remarks.

## II. RELATED WORKS

For convenience, Table I lists frequently used notation in this article.

### A. LRSMD Model for HSI

The LRSMD model was developed by Candès *et al.* [42]. It assumes that an observed data  $Y$  can be decomposed as a low-rank component  $L$  and a sparse component  $S$ . Based on this assumption, the observed data  $Y$  can be represented as

$$Y = L + S + N \quad (1)$$

where  $N$  is a Gaussian noise term. Due to the spatial neighborhood similarity in HSIs, we can use a linear combination of several basis vectors to represent each spectral vector in the background [27]. Therefore, the background usually is of low rank. Generally, anomalies are small-region targets, compared with their surroundings. Therefore, anomalies usually have sparse property [1].

Based on the analysis above, it is natural to apply the LRSMD model to separate the sparse anomaly component and low-rank background component from HSIs. The nuclear norm  $\|\cdot\|_*$  is employed as a convex relaxation of the rank in

TABLE I  
SUMMARY OF THE NOTATION

Symbol	Meaning
$Y$	Input original HSI data
$L, S, N$	Low-rank, sparse, and Gaussian terms
$\lambda$	Regularization parameter in LRSMD
$\sigma$	Constant term in LRSMD
$G_{r,\epsilon}(P, I)$	Guided filtering operation
$P, I, O$	Guidance, input, and output images in guided filter
$w_j$	A local window centered at pixel $j$
$a_j, b_j$	Two coefficients in guided filter
$\epsilon, r$	Two regularization parameters in guided filter
$\mu_j$ and $\delta_j$	Mean and variance of $I$ in $w_j$
$X$	Dimension-reduced HSI data
$m$	Spectra dimension of $X$
$s_l$	$l$ th endmember spectra
$\omega$	Noise item
$\gamma, \phi$	Attribute thinning and thickening
$T_{area}$	Predefined logical predicate
$H, F$	Two energy terms in ERS
$\beta$	Regularization parameter in ERS
$d_n, (n=1,2,3)$	Subpixel, pixel, superpixel features
$S_n, (n=1,2,3)$	Sparse anomaly components from three features
$L_n, (z=1,2,3)$	Low-rank components from three features
$K_n, (n=1,2,3)$	Spectra dimension of three anomaly components
$D_n, (n=1,2,3)$	Three initial detection maps
$W_n, (n=1,2,3)$	Three refined weight maps
$M$	Saliency map
$Y_{pc1}$	First principal component of $Y$
$L_{ap}$	Laplacian filtering operation
$\kappa$	Square dilation
$\otimes$	Dilation operation

the low-rank background and  $l_1$  norm is employed to model the sparse property [42]. Let  $Y_k$  be the  $k$ th band image of the observed HSI data  $Y$ .  $S_k$  stands for the  $k$ th band image of the sparse anomaly component  $S$ . The LRSMD model is defined as follows:

$$\min_{L_k, S_k} \|L_k\|_* + \lambda \|S_k\|_1, \quad \text{s.t. } \|Y_k - L_k - S_k\|_F < \sigma \quad (2)$$

where  $\lambda$  is a regularization parameter, and  $\sigma$  is a constant related to the standard deviation of the Gaussian noise [42], [43].

### B. Guided Filter

In recent years, some edge-preserving filters [44]–[46] have been proposed, such as the guided filter [44], the joint bilateral filter [45], and the weighted least squares [46]. The guided filter adopts a local linear model, which has been proven to be a useful tool in image matting, upsampling, and denoising [44]. In the guided filter, the output image  $O$  can be constructed by the linear transform of the guidance image  $I$  in a local window  $w_j$  centered at pixel  $j$

$$O_i = a_j I_i + b_j \quad \forall i \in w_j \quad (3)$$

where the size of  $w_j$  is  $(2r+1) \times (2r+1)$  ( $r$  decides the filter size).  $P$  is the input image. An energy function is constructed to decide coefficients  $a_j$  and  $b_j$

$$E(a_j, b_j) = \sum_{i \in w_j} ((a_j I_i + b_j - P_i) + \epsilon a_j^2) \quad (4)$$

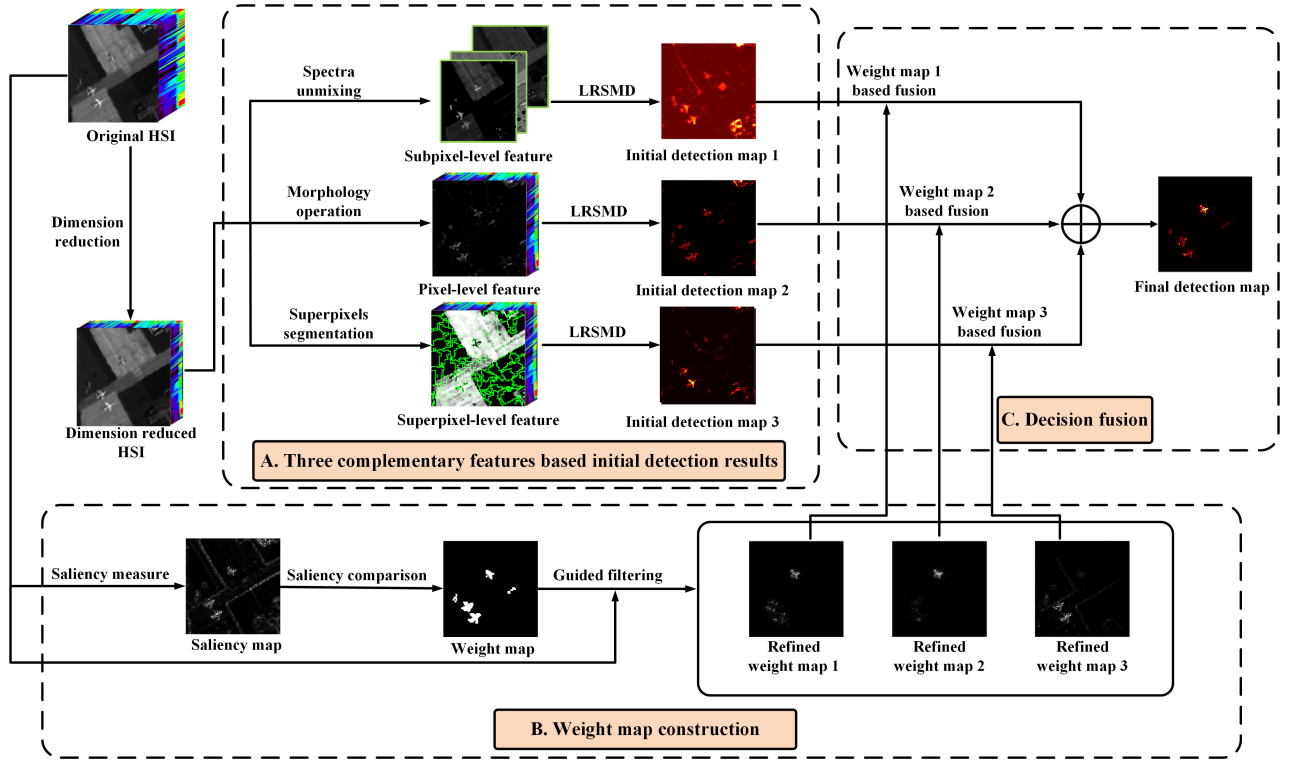


Fig. 1. Schematic of the proposed SPSGF detector.

where  $\epsilon$  decides a blurring degree of the guided filter. The coefficients  $a_j$  and  $b_j$  are solved via linear regression [44]

$$a_j = \frac{\frac{1}{|w_j|} \sum_{i \in w_j} I_i P_i - \mu_j \bar{P}_j}{\delta_j + \epsilon}, \quad b_j = \bar{P}_j - a_j \mu_j \quad (5)$$

where  $|w_j|$  denotes the number of pixels in  $w_j$ .  $\mu_j$  and  $\delta_j$  are the mean and variance of  $I$  in  $w_j$ .  $\bar{P}_j$  represents the mean of  $P$  in  $w_j$ . Then, we can calculate the output image  $O$  according to (3).

There are two goals in (4). On the one hand, the filtering output image  $a_j I_i + b_j$  needs to be as close as possible to  $P$ . On the other hand, the local linear model needs to be maintained in (4). Intensity changes in the guidance image  $I$  can be mostly preserved in  $O$  via solving (4). In this article, the guided filtering operation is represented by  $G_{r,\epsilon}(P, I)$ .

### III. SPSGF METHOD

Fig. 1 displays the schematic of the SPSGF technique. First, subpixel-, pixel-, and superpixel-level features are extracted from an HSI by employing the spectral unmixing [39], morphological operation [40], and superpixel segmentation [41] techniques, respectively. Initial detection maps can be produced from three features via employing the LRSMD technique [42]. Then, based on the spatial consistency of three features, the guided filtering-based weight optimization technique is employed to construct weight maps for fusion. Last, a simple yet effective decision fusion method is adopted to utilize the complementary information of three features, and then generates a fused detection result.

#### A. Subpixel-, Pixel-, and Superpixel-Level Features-Based Initial Detection Results

1) *Spectral Dimension Reduction*: The objective of spectral dimension reduction is to reduce the spectral dimension of HSIs, and preserve the class separability of various targets. It is helpful for HSIs processing [47]–[50] (e.g., scene classification [47] and object detection [50]). Therefore, in the proposed method, the spectral dimension of hyperspectral data is first reduced by employing the averaging fusion method [48]. Specifically, it divides an HSI into  $m$  subgroups. The  $m$ th subgroup contains  $N_m$  bands. Then, each subgroup has been fused and the resulting fused bands can be produced as follows:

$$X_m = \frac{\sum_{n=1}^{N_m} Y_m^n}{N_m} \quad (6)$$

where  $Y_m^n$  is the  $n$ th band in the  $m$ th subgroup of the input HSI  $Y$ .  $X_m$  is the  $m$ th fused band. Since the adjacent bands have the high correlation, the fused image can effectively remove the redundant information and preserve main structures for each subgroup.

2) *Spectral–Spatial Features Extraction*: By performing a spectral unmixing method, we use the fractional abundances of endmembers to represent the subpixel-level feature. According to the work [39], we employ the minimum volume simplex analysis (MVSA) approach to generate the abundance matrix  $d_1$

$$d_1 = QX \quad (7)$$

where  $X$  is the input data, which is defined as

$$X = \sum_{l=1}^e s_l(d_1)_l + \omega, \quad \text{s.t.} \quad \sum_{l=1}^e (d_1)_l = 1, \quad (d_1)_l \geq 0 \quad (8)$$

where  $s_l$  represents the  $l$ th endmembers, and  $(d_1)_l$  is the corresponding fractional abundances. The number of endmembers  $e$  is estimated by employing the vertex component analysis (VCA) [33] method. For the four data sets used in the experiment, the number of endmembers is 11, 11, 12, and 8, respectively.  $Q^{-1}$  is a mixing matrix, which is defined as

$$Q = \operatorname{argmin}_Q \log|\det(Q)|, \quad \text{s.t.} \quad QX \geq 0, \quad QX = 1 \quad (9)$$

where  $\det(Q)$  is the volume defined by the origin and the columns of  $Q$  [39]. By combining (7) and (9), the fractional abundances  $d_1$  can be estimated.

Then, we extract the pixel-level feature  $d_2$  by employing the attribute filtering operation [40]. It can adequately exploit the spatial structure information of HSIs via preserving or removing connected components. The attribute filtering results are constructed as follows:

$$AF(X_v) = [\gamma(X_v), \phi(X_v)] \quad (10)$$

where  $v$  is the  $v$ th band image of the  $X$ .  $\gamma$ ,  $\phi$ , and  $T_{\text{area}}$  represent the attribute thinnings, thickenings, and a predefined logical predicate, respectively. In real remote sensing scenes, anomalies usually are small-region targets, compared with their surroundings. To capture the area information of different objects, we employ the attribute thinning and thickening operations to remove the connected bright and dark components in an image with the predefined logical predicate, i.e.,  $\text{area} < T_{\text{area}}$  [50]. In this article,  $T_{\text{area}}$  is empirically set to 25.

After employing the attribute filtering operation, the differential operation is utilized to estimate the difference between the attribute filtered images and the input image  $X$ , which can extract anomalies from the background

$$d_2 = \sum_{v=1}^m |\phi(X_v) - X_v| + |X_v - \gamma(X_v)| \quad (11)$$

where  $s_v$  is the  $v$ th differential operation band of the dimension-reduced HSI  $X$ .  $m$  is the spectral dimension of the dimension-reduced HSI  $X$ .

To capture the superpixel-level feature  $d_3$ , we use the entropy rate superpixel (ERS) [41] technique to segment the HSI into some nonoverlapping regions. Each region is a superpixel. First, the principal component analysis (PCA) algorithm is adopted to transform  $X$  and preserve its first three principal components (PCs), which reflect the most critical information in HSIs. The extracted PCs are considered as a based image, and it is mapped to a graph. Then, the ERS algorithm is applied to generate some edges  $E_o \in E$  via solving an optimization issue

$$\max_{E_o} H(E_o) + \beta F(E_o) \quad (12)$$

where  $H$  represents the entropy rate, and  $F$  represents a balancing term. An iterative greedy algorithm [41] is employed to solve the problem (12), and the superpixel map  $o$  that

contains some homogeneous regions is produced. For the four data sets used in the experiment, the superpixel number  $N_s$  is set to 200, 200, 200, and 300, respectively. We obtain the superpixel-level feature  $d_3$  by reshaping these homogeneous regions.

3) *Initial Detection*: The LRSMD model is employed to separate the  $n$ th sparse anomaly component  $S_n$  from the  $n$ th feature  $d_n$  ( $n = 1, 2, 3$ ). We solve (2) by the alternating direction method (ADM) [43]. After the recovery of both the low-rank background components  $L_n$  and the sparse anomaly components  $S_n$ , the low-rank term contains the global background information, and the sparse term captures the anomalies information. Each band in  $S_n$  is fused together, as so to generate initial detection maps  $D_n$  ( $n = 1, 2, 3$ )

$$D_n = \frac{1}{K_n} \sum_{k=1}^{K_n} (S_n)_k \quad (13)$$

where  $K_n$  is the spectra dimension of three anomaly components  $S_n$ , and  $(S_n)_k$  is the  $k$ th band image of  $S_n$ .

### B. Weight Map Construction With Guided Filtering

The weight map in Fig. 1 is represented as follows. First, the Laplacian filter is employed to the first PC  $Y_{\text{pc1}}$  of the original image to obtain the saliency map  $M$

$$M = Y_{\text{pc1}} * L_{\text{ap}} \quad (14)$$

where  $L_{\text{ap}}$  is a  $3 \times 3$  Laplacian filter. The measured saliency map contains the saliency detail information. Then, we obtain the weight map  $W$  by thresholding the saliency map  $M$

$$W = \text{Aero}(\text{TD}(M \otimes \kappa, \theta), \zeta) \quad (15)$$

where  $\kappa$  represents a square dilation and  $\otimes$  is the dilation operation. In the function  $TD$ , a pixel is set to 1 if its value is greater than  $\theta$ , otherwise is set to 0. We adopt the well-known Otsu's method to select  $\theta$  [51]. In the function  $\text{Aero}$ , pixels in the connected component are assigned as 0, when the area is larger than  $\zeta$  pixels. When  $\zeta$  is quite large,  $\text{Aero}$  will not affect detection performances. In contrast, if  $\zeta$  is very small, anomalies and background will be both removed from the detection result. In this article, the  $\zeta$  is optimally assigned as  $N_{\text{total}}/100$  ( $N_{\text{total}}$  denotes the number of pixels in the HSI).

The obtained weight map usually contains some noise and fails to align target boundaries accurately. These factors may generate artifacts in the fused result. Employing spatial consistency is a robust strategy to tackle the issue [52], [53]. Spatial adjacent pixels usually have similar intensity values. This means that they should possess the same weight. A spatial consistency-based fusion technique is to perform the energy function, which enforces the pixel saliency and encodes edge aligned weights by a smoothness term. By minimizing the energy function, the desired weight maps can be obtained. In this article, the refined weight maps are optimized by the guided filtering. We perform the guided filter on the weight map  $W$  with the corresponding first PC  $Y_{\text{pc1}}$ . The filtering weight of the guided filter  $W_n$  ( $n = 1, 2, 3$ ) is constructed as follows:

$$W_n = G_{r_n, \epsilon_n}(W, Y_{\text{pc1}}) \quad (16)$$

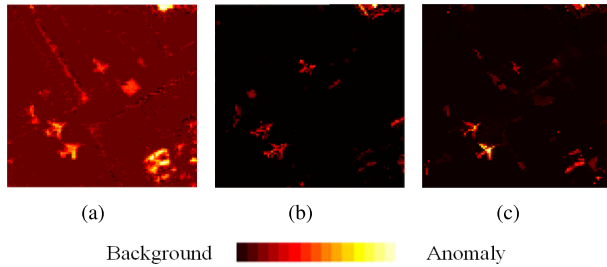


Fig. 2. Detection maps of (a) subpixel-level features, (b) pixel-level features, and (c) superpixel-level features on the San Diego data set.

where  $r_1, \epsilon_1, r_2, \epsilon_2, r_3, \epsilon_3$  represent parameters in the guided filter.  $W_1, W_2$ , and  $W_3$  mean refined weight maps of the subpixel-, pixel-, superpixel-features, respectively. Motivations of the weight construction technique are as follows. Based on (3) and (5), it is obvious that when pixels are in the flat region of the guidance image,  $a_j$  will be closed to zero and the output image  $O$  will equal  $\bar{P}_j$ . By contrast, if pixels are in the edge region,  $a_j$  will become far from zero. According to [44],  $\nabla O \approx \bar{a} \nabla I$  will achieve. This denotes that weights on the one side of the edge will be averaged. In two situations, spatial neighborhood pixels with a similar intensity value will possess similar weights.

Furthermore, in Fig. 2, the subpixel feature-based initial detection map looks spatially smooth. Therefore, the corresponding weight map needs to be smooth. Otherwise, artifacts will be generated in the fused image. On the other hand, sharp and edge-aligned weights are preferred to fuse the pixel and superpixel feature-based initial detection maps. The reason is that some image detail information may be lost if the weight map is oversmoothed. Thus, we tend to select the large filter size and the blurring degree to fuse the subpixel feature-based detection map, and we prefer to select the small filter size and the small blurring degree to fuse the pixel and superpixel features-based detection maps.

### C. Guided Filtering-Based Decision Fusion

In this step, three initial detection results  $D_n$  are fused with their corresponding weight maps  $W_n$

$$\bar{D} = \sum_{n=1}^3 W_n D_n \quad (17)$$

where  $\bar{D}$  is the final detection map. By jointly utilizing three complementary spectral-spatial features, the SPSGF method can achieve a better detection performance. The reason is that when one feature is unsatisfactory, the others may be effective.

## IV. EXPERIMENTS AND DISCUSSION

### A. Data Sets Description

Three real hyperspectral data sets and one synthetic hyperspectral data set are utilized to investigate detection performances of the SPSGF method. Four images are publicly

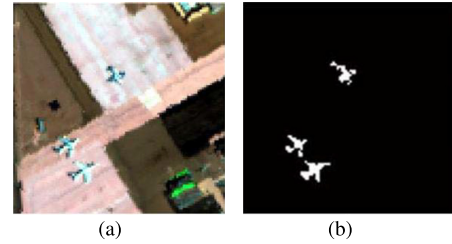


Fig. 3. San Diego data set. (a) False color image. (b) Reference detection map.

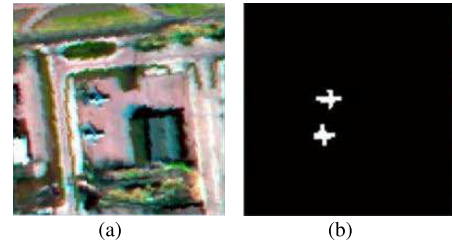


Fig. 4. ABU-airplane data set. (a) False color image. (b) Reference detection map.

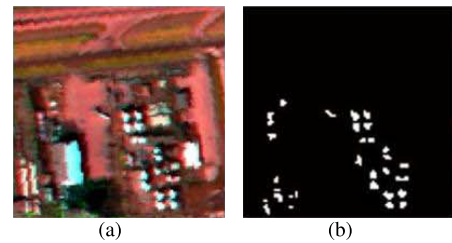


Fig. 5. ABU-Urban data set. (a) False color image. (b) Reference detection map.

available.<sup>1</sup> We have added Table II to show the important information of four data sets.

The first image was acquired by the Airborne Visible/Infrared Imaging Spectrometer (AVIRIS) sensor. It is an airport area in San Diego, CA, USA. This image has  $100 \times 100$  pixels. Its spatial resolution is 3.5 m. There are 189 spectral channels in the wavelength range of 0.37–2.51  $\mu\text{m}$ . In this data set, three aircraft are regarded as anomalies, and the surrounding background mainly consists of the airstrip and grassland. Fig. 3 shows its false color image and reference detection map.

The second image was acquired by the AVIRIS sensor. It is an airport area in Los Angeles, CA, USA. The data set comprises  $100 \times 100$  pixels. Its spatial resolution is 7.1 m. It has 205 spectral channels in the wavelength range of 0.43–0.86  $\mu\text{m}$ . Fig. 4 illustrates its false color image and reference detection map.

The third image was captured by the AVIRIS sensor. It is an urban area in Los Angeles, CA, USA. This image comprises  $100 \times 100$  pixels. The spatial resolution is 7.1 m. It has 205 spectral bands in the wavelength range of 0.43–0.86  $\mu\text{m}$ .

<sup>1</sup><http://xudongkang.weebly.com>

TABLE II  
SOME FEATURES OF THE FOUR DATA SETS

Images	Captured place	Spatial resolution	Wavelength range	Size
San Diego	San Diego	3.5m	0.37-2.51um	100 × 100 × 189
ABU-Airport	Los Angeles	7.1m	0.43-0.86um	100 × 100 × 205
ABU-Urban	Los Angeles	7.1m	0.43-0.86um	100 × 100 × 205
Gulf of Mexico	Gulf of Mexico	7.5m	0.36-2.50um	280 × 180 × 258

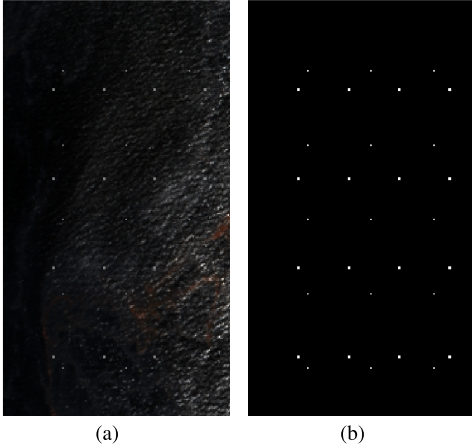


Fig. 6. Gulf of Mexico data set. (a) False color image. (b) Reference detection map.

Fig. 5 displays its false color image and reference detection map.

The fourth image was captured by the AVIRIS sensor. It is an area in the Gulf of Mexico. This image has  $280 \times 180$  pixels and 258 spectral bands that range from 0.36 to  $2.50 \mu\text{m}$ . The spatial resolution is 7.5 m. The background mainly consists of seawater and oil film. It is a challenging image since the interference of sunglint. A target implantation approach [54] is used to simulate the anomaly pixels. The synthetic subpixel anomaly objects  $x$  can be produced by implanting a desired anomalous target with spectral  $t$  in a given pixel of background with spectral  $q$  [54]

$$x = c * t + (1 - c) * q \quad (18)$$

where the AF  $c$  is 0.5. The size of these targets is  $1 \times 1$  and  $2 \times 2$ . These anomaly targets comprise 79 pixels, which account for 0.15% of the image. Fig. 6 shows its false color image and reference detection map.

### B. Detection Performance

To demonstrate the advantage of the SPSGF detector, five outstanding detectors, including RX detector [14], local RX (LRX) detector [14], collaborative representation detector (CRD) [26], LRSMD-based Mahalanobis-distance anomaly detector (LSMAD) [27], and attribute and edge-preserving filtering-based anomaly detector (AED) [50] are used for comparison. Moreover, we develop a subpixel-pixel-superpixel fusion (SPSF) method to exploit the complementary information from three features, by employing an average fusion technique. The SPSF detector is compared with the SPSGF

detector to demonstrate the advantage of the guided filtering-based fusion technique. For the sake of fairness, the setting of these parameters in the SPSF method is the same as the SPSGF method.

Receiver operating characteristic (ROC) curves [26] are adopted to evaluate the detection performance. For an ROC curve, its target detection rates and false alarm rates are computed by using a certain segmentation threshold [26]. Generally, a better detector can lead to a larger area under the curve [27]. As suggested in [55], we also calculate the area under the ROC curve (AUC) to evaluate performances of these detection methods. A better detection method usually possesses a higher AUC score.

The inner window size in the LRX detector  $w_{in}$  varies from 3 to 19, and the outer window size  $w_{out}$  varies from 5 to 23. The rank  $r$  in the LSMAD method is set to 5. The regularization parameter  $\lambda$  in the CRD approach is fixed as  $10^{-6}$ . Two filtering parameters in the AED method  $f_1$  and  $f_2$  are set to 5 and 0.5. For the SPSGF detector, a parameter setting  $K_0 = 30$ ,  $\lambda = 0.6$ ,  $T_{area} = 25$  is adopted for the test images.

For the four images, the detection results are displayed in Figs. 7–10. We can observe that the SPSGF and SPSF methods can identify the anomalies in four data sets effectively. The reason is that the SPSGF and SPSF methods can exploit jointly the complementary information of three features, instead of a single pixel-level feature. For the San Diego data set and ABU-Airport data set, the SPSGF and SPSF methods can well detect aircraft in the airstrip. By contrast, the LRX method does not perform well. The RX and CRD methods can identify the position of anomaly targets, but the shape of targets fails to be preserved effectively. Meanwhile, for the LSMAD method, edge details of some targets are lost. The reported AUC values on the San Diego image also support this observation.

For the ABU-Urban data set, the RX and LRX methods lack the robustness for detecting anomalies in the complex background, failing to identify some targets effectively. For the CRD and LSMAD methods, some background pixels are mistakenly considered as targets. Compared with the SPSF method, the SPSGF method can better highlight anomaly targets and suppress the interferences of background signals.

For the Gulf of Mexico data set, the RX, CRD, and LSMAD approaches can detect targets, but intensities are lower than the SPSGF approach. The AED and SPSF methods fail to remove interferences of the background pixels effectively. As illustrated in Table II, the proposed detector can better detect anomalies in the complex background and achieve the highest detection value,  $\text{AUC} = 0.9988$ .

The AUC scores for four data sets are illustrated in Table III. We can observe that the SPSGF detector can provide a

TABLE III  
EVALUATION SCORES ON THE FOUR DATA SETS (THE BEST RESULT IS LABELED IN BOLD)

Method	RX [14]	LRX [14]	CRD [26]	LSMAD [27]	AED [50]	SPSF	SPSGF
San Diego	0.9403	0.9457	0.9514	0.9788	0.9837	0.9812	<b>0.9921</b>
ABU-Airport	0.8404	0.9738	0.9702	0.9485	0.9901	0.9793	<b>0.9908</b>
ABU-Urban	0.9692	0.9539	0.9521	0.9607	0.9818	0.9802	<b>0.9852</b>
Gulf of Mexico	0.9910	0.9377	0.9804	0.9884	0.9927	0.9971	<b>0.9988</b>

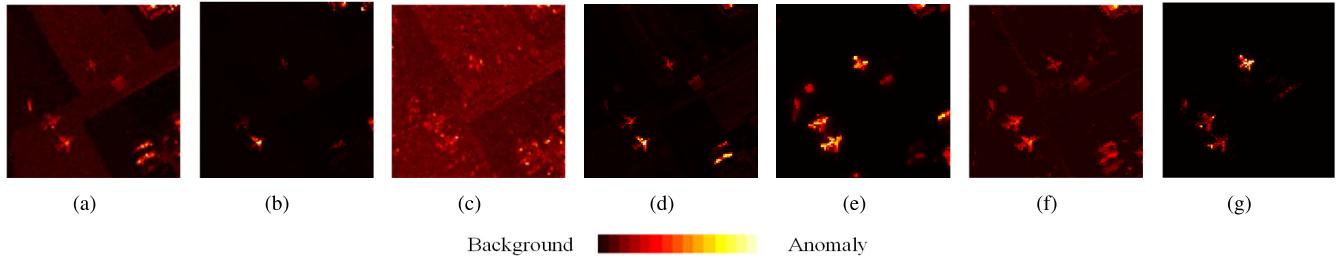


Fig. 7. Detection maps obtained by different methods for the San Diego scene. (a) RX [14]. (b) LRX [14]. (c) CRD [26]. (d) LSMAD [27]. (e) AED [50]. (f) SPSF. (g) SPSGF.

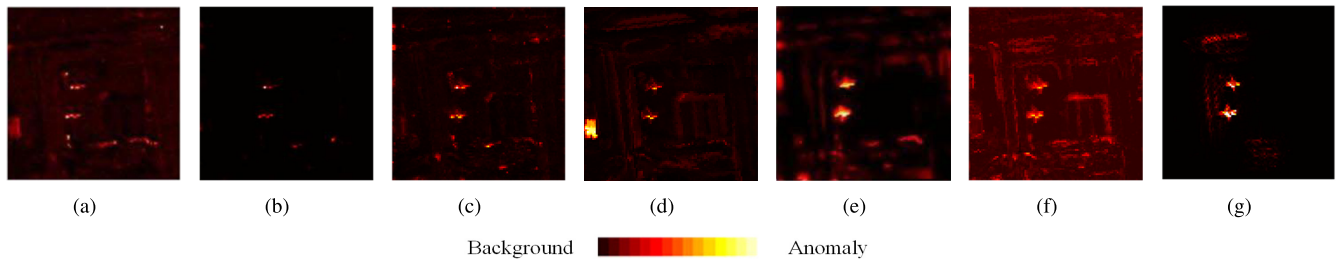


Fig. 8. Detection maps obtained by different methods for the ABU-airplane scene. (a) RX [14]. (b) LRX [14]. (c) CRD [26]. (d) LSMAD [27]. (e) AED [50]. (f) SPSF. (g) SPSGF.

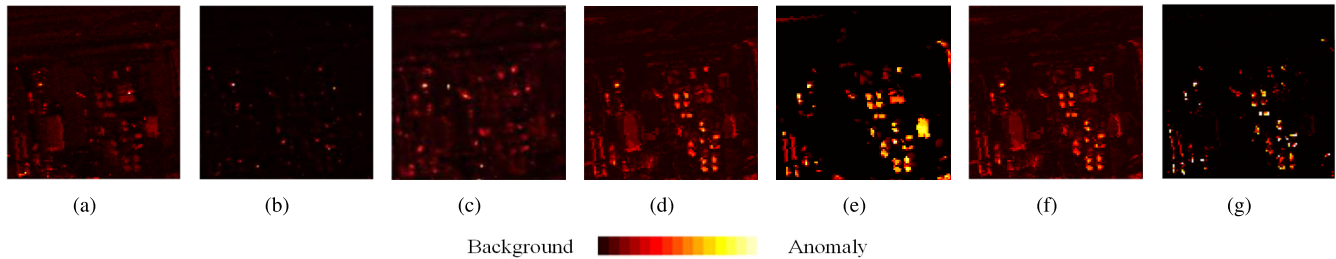


Fig. 9. Detection maps obtained by different methods for the ABU-Urban scene. (a) RX [14]. (b) LRX [14]. (c) CRD [26]. (d) LSMAD [27]. (e) AED [50]. (f) SPSF. (g) SPSGF.

better detection performance than the other methods. For four images, the AUC values obtained by the SPSGF method are 0.9921, 0.9907, 0.9852, and 0.9988, respectively. Furthermore, we compare the ROC curves of various detectors in Fig. 11. This illustrates that the SPSGF method usually has higher true-positive rates compared with others.

All the programs of various methods are executed on a computer with 2.6-GHz CPU and 32-G memory, and the test platform is MATLAB R2016b. We measure speeds of all detectors on the four data sets. The running time is presented in Table IV. We can observe that the SPSGF method needs more computational cost than the SPSF approach. The reason is that the SPSGF approach applies the guided filtering-based

weight construction technique to fuse the complementary information instead of using the simple average fusion technique. The LRX and CRD approaches need more calculating time than others.

### C. Parameters Discussion

In this section, we analyze the influence of various parameters in the SPSGF detector. Main parameters contain the band number  $m$ , sparsity regularization parameter  $\lambda$ , thresholding number  $T_{\text{area}}$ , and superpixels number  $N_s$ .

The effects of parameter  $m$  on the detection performance are illustrated in the top left of Fig. 12. When  $m = 10$ , accuracies

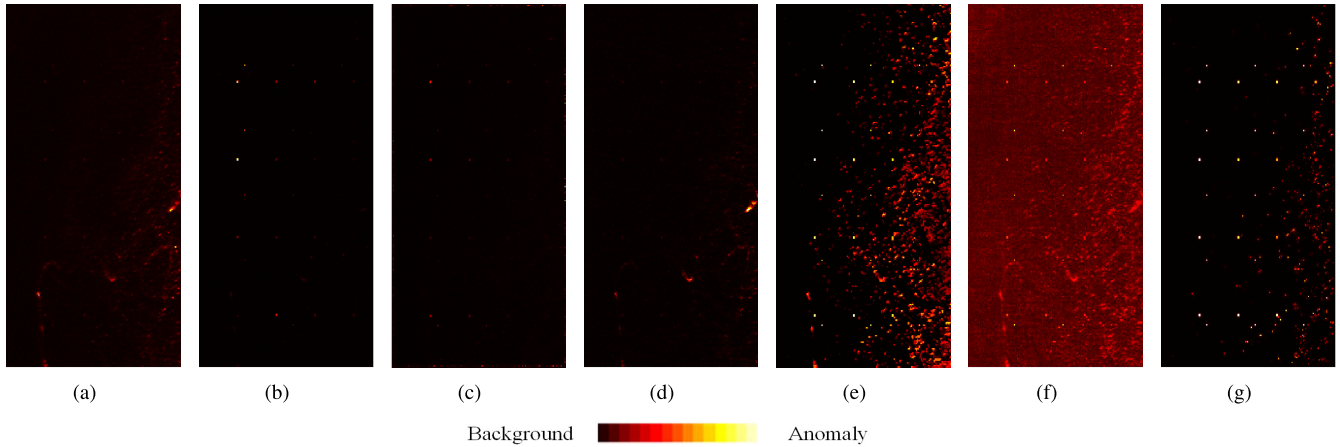


Fig. 10. Color detection maps obtained by different methods for Gulf of Mexico data set. (a) RX [14]. (b) LRX [14]. (c) CRD [26]. (d) LSMAD [27]. (e) AED [50]. (f) SPSF. (g) SPSGF.

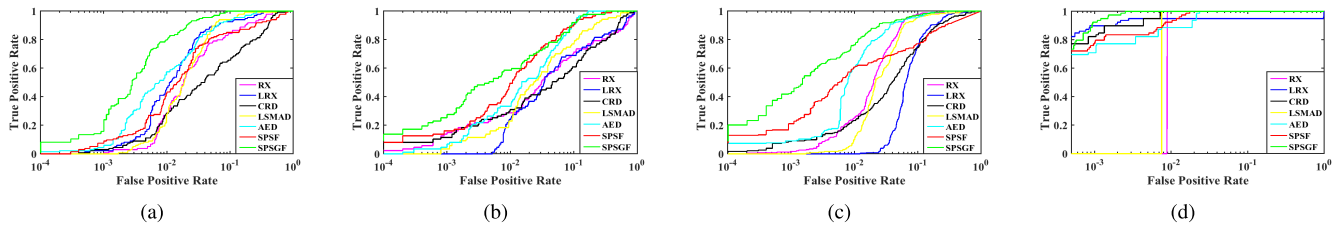


Fig. 11. ROC curves of different anomaly detection methods on four data sets. (a) San Diego scene. (b) ABU-airplane scene. (c) ABU-Urban scene. (d) Gulf of Mexico scene.

TABLE IV  
COMPUTING TIME (SECONDS) OF VARIOUS METHODS ON THE FOUR DATA SETS

Method	RX [15]	LRX [15]	CRD [27]	LSMAD [28]	AED [53]	SPSF	SPSGF
San Diego	0.28	76.23	81.76	0.83	0.61	6.35	9.23
ABU-Airport	0.29	72.46	97.76	0.86	0.62	7.24	9.87
ABU-Urban	0.31	86.97	112.97	0.84	0.64	7.03	9.31
Gulf of Mexico	1.52	453.56	671.03	2.12	1.83	47.27	51.22

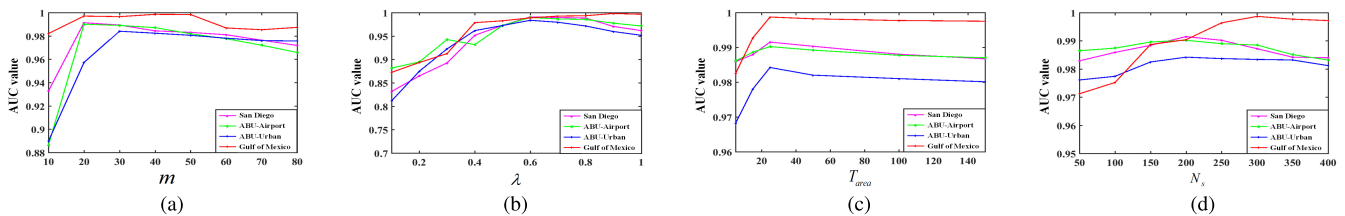


Fig. 12. Effects of main parameters on the detection performance of the proposed method. (a) Band number  $m$ . (b) Sparsity regularization  $\lambda$ . (c) Thresholding number  $T_{\text{area}}$ . (d) Superpixels number  $N_s$ .

of the SPSGF method are relatively low. The reason is that some discriminative information may be lost when  $m$  is small. The sparsity regularization parameter  $\lambda$  is set to  $q/\sqrt{N_{\text{total}}}$  (where  $N_{\text{total}}$  denotes spatial pixels in the HSI). When  $\lambda$  is larger, contributions of the sparse regularization is stronger. When  $\lambda$  is set to 0, the LRSMD solver changes to the low-rank factorization model. In both situations, the sparse anomaly components cannot be well characterized. The SPSGF method has relatively satisfactory detection performances for four test data sets when  $q$  rises from 0.5 to 0.8. The bottom subfigures illustrate the influence of  $T_{\text{area}}$  and  $N_s$ . If  $T_{\text{area}}$  is

too small, the detection accuracy will descend. The reason is that it is difficult to detect targets with the area larger than  $T_{\text{area}}$ . Moreover, if  $T_{\text{area}}$  is too large, some background regions may be detected. In addition, when  $N_s$  is quite small or large, it may fail to segment the HSIs effectively, which cannot fully reflect spectral-spatial information in homogeneous regions. According to the spatial context of three features, the parameters of the guided filter are empirically selected to  $r_1 = 33$ ,  $\epsilon_1 = 0.1$ ,  $r_2 = 8$ ,  $\epsilon_2 = 10^{-6}$ ,  $r_3 = 12$ , and  $\epsilon_3 = 10^{-5}$ .

Then, to analyze the influence of the guided filtering-based decision fusion, evaluation scores of three features,

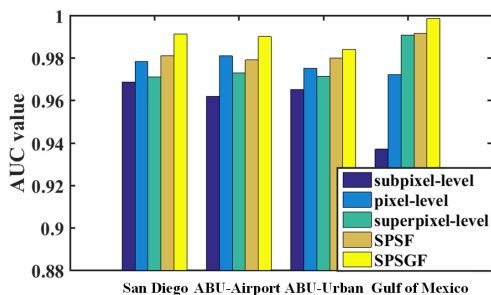


Fig. 13. Evaluation scores of the subpixel-, pixel-, superpixel-level features, SPSF method, and SPSGF method on four data sets.

SPSF method, and SPSGF method are shown in Fig. 13. Since three spectral-spatial features are captured from the same HSI, there is strong complementary information in three features. The subpixel-level feature can exploit the spectral mixture information in HSIs. The pixel-level feature can utilize the spatial structure information in HSIs. The superpixel-level feature can capture the spectral-spatial similarity information in HSIs. By combining the guided filtering-based weight constructed technique, the complementary information in three features can be better exploited for detecting anomalies.

## V. CONCLUSION

This article presents a novel SPSGF method for hyperspectral anomaly detection. The subpixel-, pixel-, superpixel-level features contain the unique spectral-spatial information in HSIs, respectively. Based on the spatial context of the three features, the guided filter is employed to construct weight maps for fusion. In this way, we can fully capture complementary information from three features for anomaly detection. Experimental results demonstrated that the SPSGF algorithm could achieve competitive detection performance on three real hyperspectral data sets and one synthetic hyperspectral data set.

In the future, we will investigate how to apply the complementary features for other applications (e.g., classification, visualization, and change detection). Moreover, deep neural network-based detection method will be furthermore researched.

## ACKNOWLEDGMENT

The authors would like to thank the Editor-in-Chief, the anonymous Associate Editor, and the Reviewers for their insightful comments and suggestions, which have greatly improved this article.

## REFERENCES

- [1] Y. Xu, Z. Wu, J. Li, A. Plaza, and Z. Wei, "Anomaly detection in hyperspectral images based on low-rank and sparse representation," *IEEE Trans. Geosci. Remote Sens.*, vol. 54, no. 4, pp. 1990–2000, Mar. 2016.
- [2] W. Xie, T. Jiang, Y. Li, X. Jia, and J. Lei, "Structure tensor and guided filtering-based algorithm for hyperspectral anomaly detection," *IEEE Trans. Geosci. Remote Sens.*, to be published, doi: [10.1109/TGRS.2018.2890212](https://doi.org/10.1109/TGRS.2018.2890212).

- [3] C.-I. Chang, Y. Wang, and S.-Y. Chen, "Anomaly detection using causal sliding windows," *IEEE J. Sel. Topics Appl. Earth Observ. Remote Sens.*, vol. 8, no. 7, pp. 3260–3270, Jul. 2015.
- [4] W. Li, G. Wu, and Q. Du, "Transferred deep learning for anomaly detection in hyperspectral imagery," *IEEE Geosci. Remote Sens. Lett.*, vol. 14, no. 5, pp. 597–601, May 2017.
- [5] Z. Shu, X. Hu, and J. Sun, "Center-point-guided proposal generation for detection of small and dense buildings in aerial imagery," *IEEE Trans. Geosci. Remote Sens.*, vol. 15, no. 7, pp. 1100–1104, Jul. 2018.
- [6] X. Zhang, G. Wen, and W. Dai, "A tensor decomposition-based anomaly detection algorithm for hyperspectral image," *IEEE Trans. Geosci. Remote Sens.*, vol. 54, no. 10, pp. 5801–5820, Oct. 2016.
- [7] Y. Yuan, D. Ma, and Q. Wang, "Hyperspectral anomaly detection by graph pixel selection," *IEEE Trans. Cybern.*, vol. 46, no. 12, pp. 3123–3134, Dec. 2016.
- [8] N. Huyan, X. Zhang, H. Zhou, and L. Jiao, "Hyperspectral anomaly detection via background and potential anomaly dictionaries construction," *IEEE Trans. Geosci. Remote Sens.*, vol. 57, no. 4, pp. 2263–2276, Apr. 2019.
- [9] D. Manolakis, D. Marden, and G. A. Shaw, "Hyperspectral image processing for automatic target detection applications," *Lincoln Lab. J.*, vol. 14, no. 1, pp. 79–116, 2003.
- [10] S. Li, K. Zhang, Q. Hao, P. Duan, and X. Kang, "Hyperspectral anomaly detection with multiscale attribute and edge-preserving filters," *IEEE Geosci. Remote Sens. Lett.*, vol. 15, no. 10, pp. 1605–1609, Oct. 2018.
- [11] Z. Huang and S. Li, "From difference to similarity: A manifold ranking based hyperspectral anomaly detection framework," *IEEE Trans. Geosci. Remote Sens.*, vol. 57, no. 10, pp. 8118–8130, Oct. 2019.
- [12] J. E. Fowler and Q. Du, "Anomaly detection and reconstruction from random projections," *IEEE Trans. Image Process.*, vol. 21, no. 1, pp. 184–195, Jan. 2012.
- [13] S. Matteoli, M. Diani, and G. Corsini, "A tutorial overview of anomaly detection in hyperspectral images," *IEEE Aerosp. Electron. Syst. Mag.*, vol. 25, no. 7, pp. 5–28, Jul. 2010.
- [14] I. S. Reed and X. Yu, "Adaptive multiple-band CFAR detection of an optical pattern with unknown spectral distribution," *IEEE Trans. Acoust. Speech Signal Process.*, vol. 38, no. 10, pp. 1760–1770, Oct. 1990.
- [15] N. M. Nasrabadi, "Regularization for spectral matched filter and RX anomaly detector," *Proc. SPIE*, vol. 6966, Apr. 2008, Art. no. 696604.
- [16] Q. Guo, B. Zhang, Q. Ran, L. Gao, J. Li, and A. Plaza, "Weighted-RXD and linear filter-based RXD: Improving background statistics estimation for anomaly detection in hyperspectral imagery," *IEEE J. Sel. Topics Appl. Earth Observ. Remote Sens.*, vol. 7, no. 6, pp. 2351–2366, Jun. 2014.
- [17] H. Kwon and N. M. Nasrabadi, "Kernel RX-algorithm: A nonlinear anomaly detector for hyperspectral imagery," *IEEE Trans. Geosci. Remote Sens.*, vol. 43, no. 2, pp. 388–397, Feb. 2005.
- [18] H. Goldberg, H. Kwon, and N. M. Nasrabadi, "Kernel eigenspace separation transform for subspace anomaly detection in hyperspectral imagery," *IEEE Geosci. Remote Sens. Lett.*, vol. 4, no. 4, pp. 581–585, Oct. 2007.
- [19] M. J. Carlotto, "A cluster-based approach for detecting man-made objects and changes in imagery," *IEEE Trans. Geosci. Remote Sens.*, vol. 43, no. 2, pp. 374–387, Feb. 2005.
- [20] S. Matteoli, M. Diani, and G. Corsini, "Improved estimation of local background covariance matrix for anomaly detection in hyperspectral images," *Opt. Eng.*, vol. 49, no. 4, pp. 1–16, Apr. 2010.
- [21] R. Zhao, B. Du, and L. Zhang, "A robust nonlinear hyperspectral anomaly detection approach," *IEEE J. Sel. Topics Appl. Earth Observ. Remote Sens.*, vol. 7, no. 4, pp. 1227–1234, Apr. 2014.
- [22] B. Du and L. Zhang, "A discriminative metric learning based anomaly detection method," *IEEE Trans. Geosci. Remote Sens.*, vol. 52, no. 11, pp. 6844–6857, Nov. 2014.
- [23] L. Gao, Q. Guo, A. Plaza, J. Li, and B. Zhang, "Probabilistic anomaly detector for remotely sensed hyperspectral data," *J. Appl. Remote Sens.*, vol. 8, no. 1, Nov. 2014, Art. no. 083538.
- [24] K. I. Ranney and M. Soumekh, "Hyperspectral anomaly detection within the signal subspace," *IEEE Geosci. Remote Sens. Lett.*, vol. 3, no. 3, pp. 312–316, Jul. 2006.
- [25] J. Li, H. Zhang, L. Zhang, and L. Ma, "Hyperspectral anomaly detection by the use of background joint sparse representation," *IEEE J. Sel. Topics Appl. Earth Observ. Remote Sens.*, vol. 8, no. 6, pp. 2523–2533, Jun. 2015.
- [26] L. Wei and D. Qian, "Collaborative representation for hyperspectral anomaly detection," *IEEE Trans. Geosci. Remote Sens.*, vol. 53, no. 3, pp. 1463–1474, Mar. 2015.

- [27] Y. Zhang, B. Du, L. Zhang, and S. Wang, "A low-rank and sparse matrix decomposition-based Mahalanobis distance method for hyperspectral anomaly detection," *IEEE Trans. Geosci. Remote Sens.*, vol. 54, no. 3, pp. 1376–1389, Mar. 2016.
- [28] I. Dopido, A. Villa, A. Plaza, and P. Gamba, "A quantitative and comparative assessment of unmixing-based feature extraction techniques for hyperspectral image classification," *IEEE J. Sel. Topics Appl. Earth Observ. Remote Sens.*, vol. 5, no. 2, pp. 421–435, Apr. 2012.
- [29] X. Xu, Y. Zhong, and L. Zhang, "Adaptive subpixel mapping based on a multiagent system for remote-sensing imagery," *IEEE Trans. Geosci. Remote Sens.*, vol. 52, no. 2, pp. 787–804, Feb. 2014.
- [30] A. Villa, J. Chanussot, J. A. Benediktsson, and C. Jutten, "Spectral unmixing for the classification of hyperspectral images at a finer spatial resolution," *IEEE J. Sel. Topics Signal Process.*, vol. 5, no. 3, pp. 521–533, Jun. 2011.
- [31] X. Li, X. Jia, L. Wang, and K. Zhao, "On spectral unmixing resolution using extended support vector machines," *IEEE Trans. Geosci. Remote Sens.*, vol. 53, no. 9, pp. 4985–4996, Sep. 2015.
- [32] M.-D. Iordache, J. Bioucas-Dias, and A. Plaza, "Sparse unmixing of hyperspectral data," *IEEE Trans. Geosci. Remote Sens.*, vol. 49, no. 6, pp. 2014–2039, Jun. 2011.
- [33] J. M. P. Nascimento and J. M. Bioucas-Dias, "Vertex component analysis: A fast algorithm to unmix hyperspectral data," *IEEE Trans. Geosci. Remote Sens.*, vol. 43, no. 4, pp. 898–910, Apr. 2005.
- [34] T. Lu, S. Li, L. Fang, X. Jia, and J. A. Benediktsson, "From subpixel to superpixel: A novel fusion framework for hyperspectral image classification," *IEEE Trans. Geosci. Remote Sens.*, vol. 55, no. 8, pp. 4398–4411, Aug. 2017.
- [35] L. Y. Fang, S. T. Li, X. D. Kang, and J. A. Benediktsson, "Spectral-spatial classification of hyperspectral images with a superpixel-based discriminative sparse model," *IEEE Trans. Geosci. Remote Sens.*, vol. 53, no. 8, pp. 4186–4201, Aug. 2015.
- [36] L. Fang, S. Li, W. Duan, J. Ren, and J. A. Benediktsson, "Classification of hyperspectral images by exploiting spectral–spatial information of superpixel via multiple kernels," *IEEE Trans. Geosci. Remote Sens.*, vol. 53, no. 12, pp. 6663–6674, Dec. 2015.
- [37] T. Priya, S. Prasad, and H. Wu, "Superpixels for spatially reinforced Bayesian classification of hyperspectral images," *IEEE Geosci. Remote Sens. Lett.*, vol. 12, no. 5, pp. 1071–1075, May 2015.
- [38] J. Li, H. Zhang, and L. Zhang, "Efficient superpixel-level multitask joint sparse representation for hyperspectral image classification," *IEEE Trans. Geosci. Remote Sens.*, vol. 53, no. 10, pp. 5338–5351, Oct. 2015.
- [39] J. Li, A. Agathos, D. Zaharie, J. M. B. Dias, A. Plaza, and X. Li, "Minimum volume simplex analysis: A fast algorithm for linear hyperspectral unmixing," *IEEE Trans. Geosci. Remote Sens.*, vol. 53, no. 9, pp. 5067–5082, Sep. 2015.
- [40] E. J. Breen and R. Jones, "Attribute openings, thinnings, and granulometries," *Comput. Vis. Image Understand.*, vol. 64, no. 3, pp. 377–389, Nov. 1996.
- [41] M.-Y. Liu, O. Tuzel, S. Ramalingam, and R. Chellappa, "Entropy rate superpixel segmentation," in *Proc. IEEE Conf. Comput. Vis. Pattern Recognit.*, Jun. 2011, pp. 2097–2104.
- [42] E. J. Candès, X. Li, Y. Ma, and J. Wright, "Robust principal component analysis," *J. ACM*, vol. 58, no. 3, pp. 1–37, May 2011.
- [43] X. Yuan and J. Yang, "Sparse and low-rank matrix decomposition via alternating direction methods," *Pacific J. Optim.*, vol. 9, no. 1, pp. 167–180, 2013.
- [44] K. He, J. Sun, and X. Tang, "Guided image filtering," in *Proc. Eur. Conf. Comput. Vis.*, 2010, pp. 1–14.
- [45] F. Durand and J. Dorsey, "Fast bilateral filtering for the display of high-dynamic-range images," *ACM Trans. Graph.*, vol. 21, no. 3, pp. 257–266, 2002.
- [46] Z. Farbman, D. Lischinski, and R. Szeliski, "Edge-preserving decompositions for multi-scale tone and detail manipulation," *Trans. Graph.*, vol. 27, no. 3, p. 67, Aug. 2008.
- [47] Y. Zhou, J. Peng, and C. L. P. Chen, "Dimension reduction using spatial and spectral regularized local discriminant embedding for hyperspectral image classification," *IEEE Trans. Geosci. Remote Sens.*, vol. 53, no. 2, pp. 1082–1095, Feb. 2015.
- [48] X. Kang, X. Xiang, S. Li, and J. A. Benediktsson, "PCA-based edge preserving features for hyperspectral image classification," *IEEE Trans. Geosci. Remote Sens.*, vol. 55, no. 12, pp. 7140–7150, Dec. 2017.
- [49] G. Liccardi, P. R. Marpu, J. Chanussot, and J. A. Benediktsson, "Linear versus nonlinear PCA for the classification of hyperspectral data based on the extended morphological profiles," *IEEE Geosci. Remote Sens. Lett.*, vol. 9, no. 3, pp. 447–451, May 2012.
- [50] X. Kang, X. Zhang, S. Li, K. Li, J. Li, and J. A. Benediktsson, "Hyperspectral anomaly detection with attribute and edge-preserving filters," *IEEE Trans. Geosci. Remote Sens.*, vol. 55, no. 10, pp. 5600–5611, Oct. 2017.
- [51] N. Otsu, "A threshold selection method from gray-level histograms," *IEEE Trans. Syst., Man, Cybern.*, vol. SMC-9, no. 1, pp. 62–66, Jan. 1979.
- [52] W. Liao *et al.*, "Two-stage fusion of thermal hyperspectral and visible RGB image by PCA and guided filter," in *Proc. 7th Workshop Hyperspectral Image Signal Process., Evol. Remote Sens. (WHISPERS)*, Jun. 2015, pp. 1–4.
- [53] S. Li, X. Kang, and J. Hu, "Image fusion with guided filtering," *IEEE Trans. Image Process.*, vol. 22, no. 7, pp. 2864–2875, Jul. 2013.
- [54] D. W. J. Stein, S. G. Beaven, L. E. Hoff, E. M. Winter, A. P. Schaum, and A. D. Stocker, "Anomaly detection from hyperspectral imagery," *IEEE Signal Process. Mag.*, vol. 19, no. 1, pp. 58–69, Jan. 2002.
- [55] L. Wang *et al.*, "Band subset selection for anomaly detection in hyperspectral imagery," *IEEE Trans. Geosci. Remote Sens.*, vol. 55, no. 9, pp. 4887–4898, Sep. 2017.



**Zhihong Huang** (Student Member, IEEE) received the B.S. degree from the Hunan University of Science and Technology, Xiangtan, China, in 2015. He is currently pursuing the Ph.D. degree with the Laboratory of Vision and Image Processing, Hunan University, Changsha, China.

His research interests include remote sensing image denoising, scene classification, and remote sensing object detection.



**Leyuan Fang** (Senior Member, IEEE) received the Ph.D. degree from the College of Electrical and Information Engineering, Hunan University, Changsha, China, in 2015.

From September 2011 to September 2012, he was a Visiting Ph.D. Student with the Department of Ophthalmology, Duke University, Durham, NC, USA, supported by the China Scholarship Council. From August 2016 to September 2017, he was a Post-Doctoral Research Fellow with the Department of Biomedical Engineering, Duke University. Since

January 2017, he has been an Associate Professor with the College of Electrical and Information Engineering, Hunan University. His research interests include sparse representation and multiresolution analysis in remote sensing and medical image processing.

Dr. Fang received the Scholarship Award for Excellent Doctoral Student granted by the Chinese Ministry of Education in 2011.



**Shutao Li** (Fellow, IEEE) received the B.S., M.S., and Ph.D. degrees from Hunan University, Changsha, China, in 1995, 1997, and 2001, respectively.

In 2001, he joined the College of Electrical and Information Engineering, Hunan University. From May 2001 to October 2001, he was a Research Associate with the Department of Computer Science, The Hong Kong University of Science and Technology, Hong Kong. From November 2002 to November 2003, he was a Post-Doctoral Fellow with the Royal Holloway College, University of London, London, U.K. From April 2005 to June 2005, he was a Visiting Professor with the Department of Computer Science, The Hong Kong University of Science and Technology. He is currently a Full Professor with the College of Electrical and Information Engineering, Hunan University. He has authored or coauthored over 200 refereed articles. His current research interests include image processing, pattern recognition, and artificial intelligence.

Dr. Li is a member of the Editorial Board of *Information Fusion and Sensing and Imaging*. He received two 2nd-Grade State Scientific and Technological Progress Awards of China, in 2004 and 2006, respectively. He is an Associate Editor of the IEEE TRANSACTIONS ON GEOSCIENCE AND REMOTE SENSING and the IEEE TRANSACTIONS ON INSTRUMENTATION AND MEASUREMENT.